Geophysical Journal International

Geophys. J. Int. (2014) **197,** 1763–1769
Advance Access publication 2014 April 1

doi: 10.1093/gji/ggu087

Interaction of Cocos and Rivera plates with the upper-mantle transition zone underneath central Mexico

Xyoli Pérez-Campos[1,2] and Robert W. Clayton[2]

[1]*Departamento de Sismología, Instituto de Geofísica, Universidad Nacional Autónoma de México, Ciudad Universitaria, Coyoacán, Mexico, D. F.* 04510, *Mexico. E-mail: xyoli@geofisica.unam.mx*
[2]*Seismological Laboratory, California Institute of Technology, Pasadena, CA* 91125, *USA*

Accepted 2014 March 7. Received 2014 February 28; in original form 2013 July 25

SUMMARY

Receiver functions (RFs) from 224 permanent and temporary stations in central and southern Mexico were used to characterize the upper-mantle transition zone in that region. Discontinuities at 410 and 660 km depth are both deeper compared to iasp91, which reflects a slow velocity anomaly in the upper mantle. They show topography on the interfaces that is consistent with the interaction of the subducted slab or its broken off extension. A low-velocity layer on top of the 410 is identified mainly on the continental side of where the slab pierces it (i.e. in the lee of the slab roll-back). In general the RFs show a complex behaviour where the mantle has been disturbed by the lateral motion of the subducted slab, and are simple where it has not. Complexity on the 660 coincides with the place where the broken off portion of the Farallon Plate would have penetrated this interface or is possibly lying on top of it.

Key words: Mantle processes; Phase transitions; North America.

1 INTRODUCTION

Central Mexico is tectonically characterized by the subduction of the Cocos and Rivera plates beneath the North American Plate. Cocos and Rivera subduction started at the beginning of the Miocene, when the Farallon Plate evolved into the Guadalupe Plate which later separated into the Rivera and Cocos plates (Mammerickx & Klitgord 1982). The subduction of the East Pacific Rise produced a slab window and a slab tear that propagated laterally eastwards (Ferrari 2004), which resulted on the volcanism migration observed along the Trans Mexican Volcanic Belt (TMVB). Tomographic images suggest that Farallon continued its subduction to the east, leaving some fragments under North America (e.g. van der Lee & Nolet 1997), but generally descended to a depth of ∼1500 km below the mid-Atlantic (e.g. Grand *et al.* 1997; van der Hilst *et al.* 1997; Gorbatov *et al.* 2001).

Currently, the subduction angle varies along the trench, from a high angle in the north, to a horizontal subduction in central Mexico and back to a high angle to the south (Pardo & Suárez 1995). The slab has been rolling back for the last 20 Myr, as indicated by a southern migration of the TMVB volcanism (Ferrari *et al.* 2001; Gómez-Tuena *et al.* 2003; Orozco-Esquivel *et al.* 2007) and the lack of compressional geological features in the forearc during this time period (e.g. Nieto-Samaniego *et al.* 2006; Morán-Zenteno *et al.* 2007).

The slab geometry has been delineated by seismicity (e.g. Pardo & Suárez 1995), tomography (Gorbatov & Fukao 2005; Husker & Davis 2009; Yang *et al.* 2009) and receiver functions (RFs; Pérez-Campos *et al.* 2008; Kim *et al.* 2010; Melgar & Pérez-Campos 2011). The most striking feature of the slab is that under central Mexico, it is horizontal for 250 km from the trench (Pérez-Campos *et al.* 2008). Just before the TMVB, the slab dives steeply into the upper mantle with an angle of 70°, passing through a depth of ∼410 km at a distance of 380 km from the trench. Tomographic images indicate that the slab terminates at a depth of approximately 570 km (Husker & Davis 2009).

The goal of this work is to determine the presence of the slab in the mantle transition zone (MTZ), between the seismic discontinuities at 410 and 660 km (hereafter called the 410 and the 660, respectively), its interaction with the upper-mantle discontinuities and its role in hydrating the upper mantle in the region. Central Mexico is a good place to do this because there are fairly precise models of where the slab intersects the MTZ, and there is a reasonably dense seismic network that covers the region.

2 DATA

We use teleseismic data from six deployments in central and southern Mexico (Fig. 1):

(1) the MesoAmerican Subduction Experiment (MASE; MASE 2007),
(2) the Veracruz-Oaxaca (VEOX) experiment (VEOX 2010),
(3) the Mapping the Rivera Subduction zone (MARS) experiment (Yang *et al.* 2009),
(4) the Guerrero Gap (GGAP) project, a network focused on the non-volcanic tremors in the Guerrero region (Zigone *et al.* 2012),

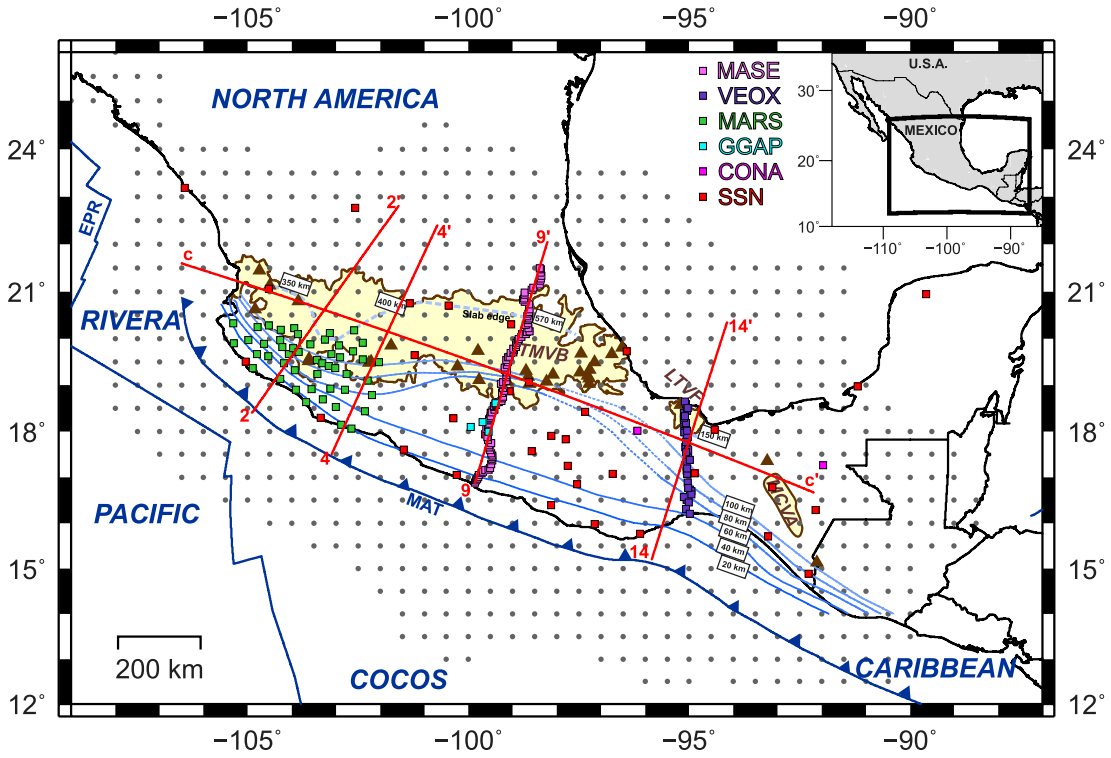

Figure 1. Station locations (squares). The yellow area denotes the current location of the TMVB, the Los Tuxtlas Volcanic Field (LTVF) and the Modern Chiapanecan Volcanic Arc (MCVA; Ferrari *et al.* 2012); brown triangles denote active volcanoes. Profiles 2, 4, 9, 14 and c are shown in Fig. 3. Grey dots denote the grid nodes for RFs stacking. MAT, Middle American Trench. Blue lines denote the isodepth contours of Rivera and Cocos slab as determined by Pardo & Suárez (1995) and modified by recent results (Pérez-Campos *et al.* 2008; Yang *et al.* 2009; Melgar & Pérez-Campos 2011). The edge of the slab with the depth it reaches is denoted by a light dashed line.

(5) two temporary stations to complement the existing SSN stations in southcentral Mexico (we will refer them as CONA), and

(6) the broad-band permanent stations in central and southern Mexico of the Servicio Sismológico Nacional (SSN, National Seismological Service in Mexico, http://www.ssn.unam.mx).

In total, we were able to obtain 6935 *P*-wave RFs from the 224 stations (Fig. S1). The noise levels at the frequency range used in this study are comparable for all data sets, including permanent and temporary stations (Fig. S1).

3 ANALYSIS OF THE CONVERTED PHASES

We employed the standard RF method (Vinnik 1977), with a 120-s data window, starting 30 s before the *P*-wave onset. The three components of the seismogram *Z*-vertical, *N*-North and *E*-East are rotated to a *P*-polarization ray-based coordinate system *L*-longitudinal, *Q*-radial and *T*-transversal by finding the eigenvectors of the covariance matrix and minimizing the rotation (Kanasewich 1973; Husebye *et al.* 1975; Vinnik 1977). We then performed the deconvolution of the *Q* component by the *L* component in the time domain (Ligorría & Ammon 1999), using a Gaussian filter with a width parameter of 2.5. We kept only the best RFs based on the fit of the estimated *Q* component to the convolution of the estimated RF and the *L* component, retaining only those with 70 per cent or higher semblance; no difference in the results is observed if a higher level of semblance is chosen. In order to enhance the mantle discontinuity arrivals, we further filtered the RFs between 0.025 and 0.3 Hz (Fig. S1).

Following Dueker & Sheehan (1997), we stacked the RFs according to their common conversion points (CCPs). We used iasp91 (Kennett & Engdahl 1991) as the reference velocity model to backproject the RFs along their ray paths and identify their conversion points at the 410 and the 660 discontinuities. We are interested on the relative behaviour of the discontinuities rather than their absolute depth, therefore correction for a 3-D structure is not essential and the results presented here are referenced to the velocity model used for the backprojection. Anomalies in the upper mantle will translate to a shift in depth for both discontinuities, while small lateral heterogeneities will increase our error estimation (∼7 km) of the discontinuity depth (e.g. Gurrola & Minster 1998; Owens *et al.* 2000). Based on Gilbert *et al.* (2003), we stacked the RFs within a distance of 1.5° from each node of a 0.5° × 0.5° grid, for each discontinuity. The minimum number allowed for the stacking is 10 (Fig. 2). We obtained the mean of the stack and its confidence interval (Fig. 3) by bootstrapping the RFs at each node (Efron & Tibshirani 1993). We only interpret our results within the region outlined by the purple line in Fig. 2, which corresponds to nodes where at least 10 different stations contribute to the RFs stack. Furthermore, the region within the white line in Fig. 2 corresponds to nodes with an azimuthal gap less than 180°. The gap is due to a lack of earthquakes from the NE.

The discontinuities are first determined by means of an automatic picker, which looks for peaks that exceed 80 per cent of maximum value within the selected range interval (360–460 for the 410, and 610–710 for the 660). The maximum of these peaks is selected as a candidate for the converted phase for the discontinuity. We then do a thorough visual inspection for lateral coherence, and the pick selections were modified accordingly. Deviations from the

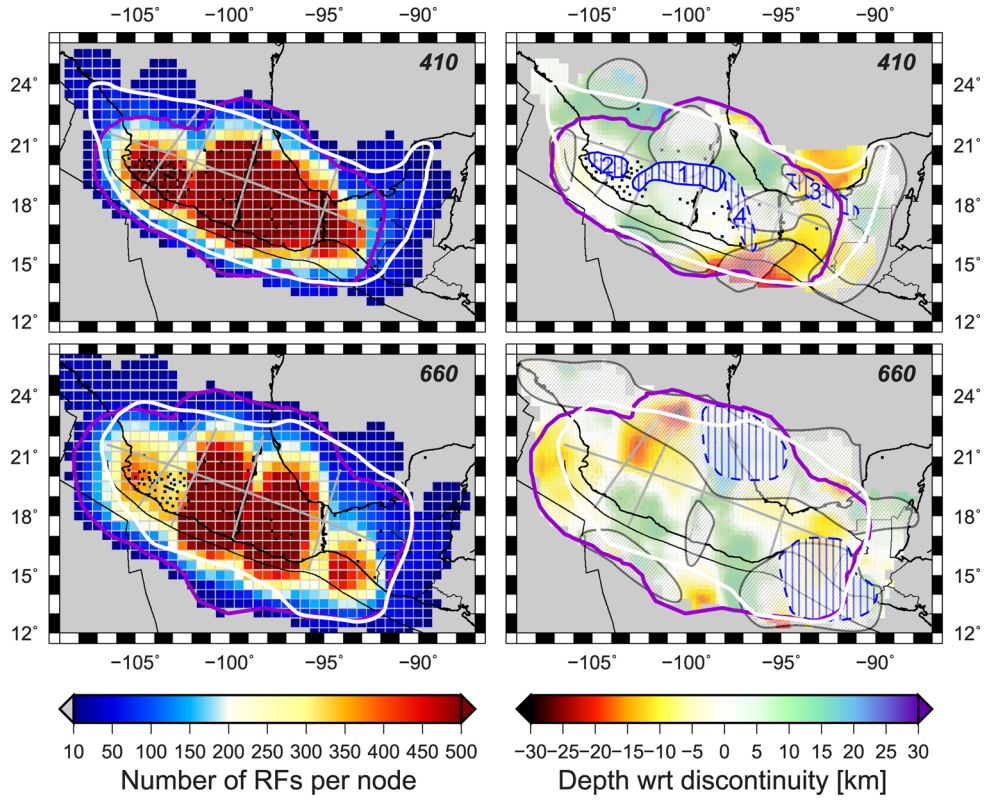

Figure 2. Left-hand side: Number of RFs per node for the 410 (top panel) and the 660 (bottom panel). The minimum allowed for the stacking was 10. The purple line denotes the area within at least 10 different stations contributing with RFs for the stack. The white line denotes the area within the nodes having an azimuthal gap less than 180°. Right-hand side: Topography of the 410 (top panel) and 660 (bottom panel). The colour corresponds to the depth with respect to a mean depth of 421 km for the 410 and of 676 km for the 660. The grey-hashed regions denote regions where the RFs were considered complex and the blue hashed regions denote the presence of slab material (1: Husker & Davis 2009; 2: Yang *et al.* 2009; 3: Gorbatov & Fukao 2005; 4: our interpretation, see text). Grey lines show the position of profiles 2, 4, 9, 14 and c for Fig. 3.

automatic picking to the final picking depend on the complexity of the RF.

To assess complexity in the RFs we used the number of peaks and valleys (NPV) for the mean RF at each node, as done by Pérez-Campos & Clayton (2013). NPV is defined as the number of maxima and minima that exceed 80 per cent of the maximum value observed in the RF, as long as it has a zero crossing in between. The bootstrap errors of the RFs at each node are small enough to disregard them when estimating the NPV. In Fig. 2, we represent regions with complex RFs (NPV ≥ 4) as grey-hashed regions.

The slab presence could hydrate the MTZ, resulting in a low-velocity layer (LVL) above the 410 (Bercovici & Karato 2003) and a garnet-rich mantle. The first one will result on a negative phase in the RFs above the main arrival for the *P*410*s* and the second one will generate complex arrivals for the 660 (e.g. Simmons & Gurrola 2000; Ai *et al.* 2003). Therefore, the complexity suggested by the NPV might be an indicator of a presence of an LVL for the 410 or multiple phase conversions for the 660. Note that crustal multiples generated by the Moho will arrive outside the zone used to measure complexity for each of the discontinuities.

4 UPPER-MANTLE DISCONTINUITIES

The average depth of the 410 across the region is 421 ± 11, and for the 660, it is 676 ± 10 km. This means both discontinuities are shifted deeper by at least 10 km, which would reflect a slow anomaly in the upper mantle, as indicated by Li *et al.* (2008). In Fig. 2 the topography of the discontinuities is shown relative to these average depths. In relative terms, topography of the 410 shows an uplifted region with respect to the depressed surrounding, which we interpret as the place where the slab is penetrating the 410 (Fig. 2, blue hashed region marked with number 1). This corresponds to the position where Husker & Davis (2009) found the slab at 410 km depth along the MASE line in central Mexico. Another similar region is also observed to the northwest, which corresponds to the position where the slab reaches 410 km depth in the tomography by Yang *et al.* (2009; Fig. 2, blue hashed region marked with number 2). To the east, there is also an uplifted region, shown with warm colours in Fig. 2 and a corresponding blue hashed region marked with number 3. This region corresponds to the presence of cold material according to seismic tomography by Gorbatov & Fukao (2005) and the global tomography by Li *et al.* (2008). The penetration of the slab through the 410 is characterized by simple RFs with diminished amplitude (Fig. 3). This is similar to observations by Li *et al.* (2000), who observed a gap in the RF image around the 410 where the Pacific slab penetrates to the MTZ. They suggested that the variability in the topography due to the presence of the slab might not be resolvable by their data. On the north side of the slab (i.e. in the lee of the lateral movement of the slab), the RFs show a complex behaviour. By following both criteria—simplicity of the RFs and a locally uplifted region—we identified the possible position of another fragment of the slab reaching the 410, which is marked with blue-hashed region number 4 in Fig. 2.

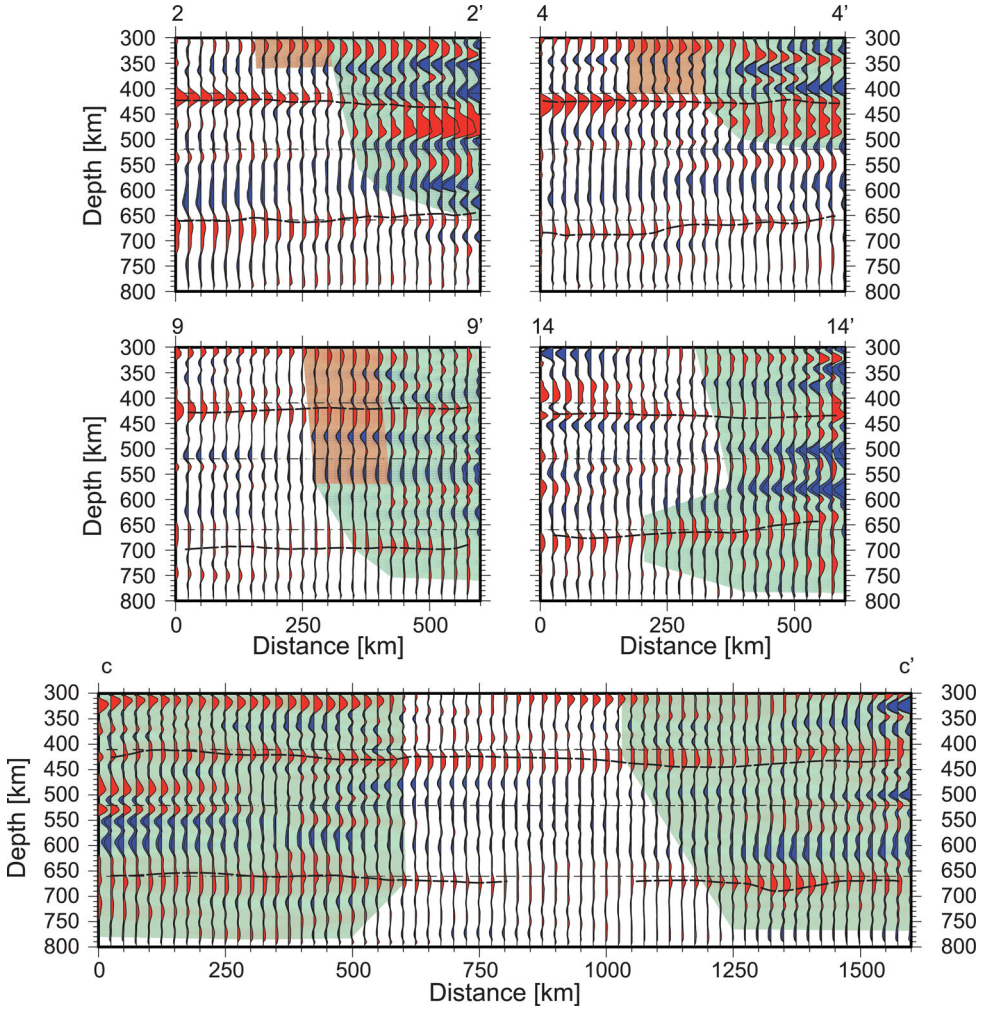

Figure 3. Profiles transverse to the slab (2, 4, 9 and 14) and longitudinal to the slab (c, see Fig. 1). Each RF shows the stack and its confidence interval. Brown areas correspond to the slab according to Yang *et al.* (2009) for profiles 2 and 4, and to Husker & Davis (2009) for profile 9. Green areas denote regions of complex RFs. Black dashed lines denote our interpretation for the 410 and the 660.

The 660 discontinuity shows three regions where it is depressed, with one north and one south of the MASE line, and the third one in southern Mexico. The first and third, along with the complex nature of the RFs, indicate the possibility of cold material sitting on top of the 660 discontinuity. East of the MASE line, Gorbatov & Fukao (2005) show a fast anomaly lying horizontally for ∼600 km to the northeast and then penetrating to the lower mantle. For southern Mexico, the fast anomaly seems to penetrate the 660 at ∼300 km from the trench (Gorbatov & Fukao 2005).

In general, the MTZ under central Mexico, south of the TMVB appears to be affected by the presence of cold material, making it slightly thicker (∼15 km) than the global average. This is correlated with the interaction of the Cocos slab with the MTZ. While to the east of the TMVB, the MTZ undergoes a thin–thick–thin change in thickness. This is the region where the Cocos slab appears to have broken off (Rogers *et al.* 2002), and this may be the cause of the changes in the MTZ. This is also where the volcanic arc almost disappears in the transition from the TMVB to the MCVA.

Fig. 3 shows four profiles from west through east that cut the slab in a transverse direction, and one profile in the longitudinal direction. Additional profiles are shown in Fig. S3. The 410 and 660 global discontinuities are indicated. Despite the RFs insensitivity to smooth velocity variations, there is a striking correlation between the RF nature and the tomographic images by Li *et al.* (2008) and Gorbatov & Fukao (2005). RFs in the region of fast (cold) material show a more complicated nature.

Although intermittent, an LVL is evident above the 410 discontinuity, especially near where interaction seems to occur between cold material and the 410 discontinuity (Fig. 3). The LVL zone above the 410 is also seen in a refraction study in northeastern Mexico by Gao *et al.* (2006).

5 DISCUSSION AND CONCLUSIONS

Fig. 4 summarizes our observations of the upper-mantle discontinuities under central Mexico. Cocos slab appears to interact with the MTZ in an intermittent rather than spatially continuous fashion. In central Mexico, the slab penetrates the 410 discontinuity at the location predicted by the recent seismic tomography study of Husker & Davis (2009). This tomography shows the slab truncated at 500 km, and the global tomography by Li *et al.* (2008) and the regional tomography by Gorbatov & Fukao (2005) show what is likely the broken off part of the slab interacting with the 660 discontinuity. This is consistent with the topography we observe for the 660 discontinuity north of current end of the slab. The remnant of

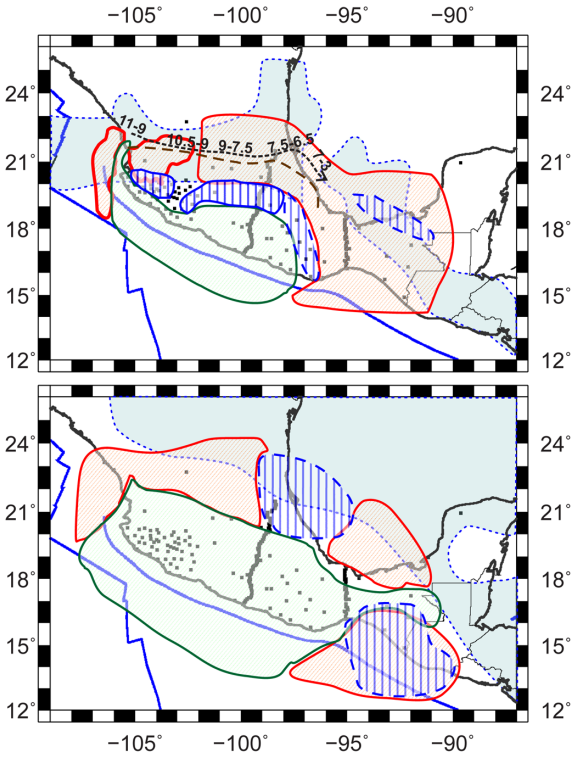

Figure 4. Interpretation. Top panel: 410. Bottom panel: 660. Blue hashed regions correspond to the presence of the slab interacting with the discontinuity as observed by Husker & Davis (2009) and Yang *et al.* (2009) and as interpreted from the RFs in this study. Red regions correspond to complex RF regions, interpreted as hydrated due to the slab, while green regions correspond to simple RF regions, where there has not been interaction of the slab. Light blue regions, outlined by a dotted line show where Farallon is observed in the tomography by Gorvatov & Fukao (2005) at a depth of 380 km (top panel) and 615 km (bottom panel). The dashed black arrow represents the progression of the slab tear and the numbers the age of this progression (Ferrari 2004).

the slab may be either sitting on top of the 660 or penetrating it. Our data do not provide the resolution to distinguish these two cases.

The LVL above the 410 seems to be the result of hydration due to the passage of the subducted slab, as seen in other places (e.g. Song *et al.* 2004; Gao *et al.* 2006; Vinnik *et al.* 2010, Schmandt *et al.* 2011; Tauzin *et al.* 2013). In a similar fashion to the complexity on the 660 interface, the LVL generally appears where the slab interacts with the 410 (i.e. where the 410 pierces it currently and in the past).

The analysis of the mantle discontinuities and transition zone in the Gulf of California (Pérez-Campos & Clayton 2013) show that the warm and hydrated system in the northern Gulf produced complex RFs (mainly for the 660 discontinuity), in contrast to the RFs in central and southern Mexico which appear much simpler and suggest the presence of cold material that is likely due to the remnant Farallon slab (Yang & Forsyth 2006). In this study the complex zones appear to be localized in regions where the interfaces have been penetrated by the Cocos slab.

In conclusion, the penetration of the 410 discontinuity by the slab appears to have hydrated the region, in such a way as to produce an LVL on top of the 410 (Bercovici & Karato 2003) starting at the point of penetration and continuing in its lee. In contrast, regions that have not been disturbed by the passing of the subducted slab show simple RFs.

ACKNOWLEDGEMENTS

Figures were done using Generic Mapping Tools (GMT; Wessel & Smith 1991). We thank C. Cárdenas and E.A. Solano for providing noise curves for the SSN. We thank all the volunteers that made possible the operation of MASE, VEOX, MARS, GGAP and CONA, and the SSN personnel for installation and maintenance of the stations and making possible data availability. CONA stations were funded by Conacyt project J51566-F. GGAP stations were funded through the Agence Nationale de la Recherche (France) under the contract RA0000CO69 (ANR G-GAP). Fund for this work was provided by DGAPA-UNAM project IN105910 and the Tectonics Observatory at Caltech, which is funded by the Betty and Gordon Moore Foundation. This is contribution #233 from the Tectonics Observatory. XP-C had a sabbatical fellowship from DGAPA-UNAM and thanks the Tectonics Observatory at Caltech for partial funding for her sabbatical. We further thank B. Tauzin and an anonymous reviewer whose comments helped improve this paper.

REFERENCES

Ai, Y., Zheng, T., Xu, W., He, Y. & Dong, D., 2003. A complex 660 km discontinuity beneath northeast China, *Earth planet. Sci. Lett.,* **212,** 63–71.

Bercovici, D. & Karato, S.-I., 2003. Whole-mantle convection and the transition-zone water filter, *Nature,* **425,** 39–44.

Dueker, K.G. & Sheehan, A.F., 1997. Mantle discontinuity structure from midpoint stacks of converted P to S waves across the Yellowstone hotspot track, *J. geophys. Res.,* **102,** 8313–8327.

Efron, B. & Tibshirani, R.J., 1993. An introduction to the bootstrap, in *Monographs on Statistics and Applied Probability,* Vol. 57, pp. 168–177, eds Cox, D.R., Hinkley, D.V., Reid, N., Rubin, D.B. & Silverman, B.W., Chapman & Hall/CRC.

Ferrari, L., 2004. Slab detachment control on mafic volcanic pulse and mantle heterogeneity in central Mexico, *Geology,* **32,** 77–80.

Ferrari, L., López-Martínez, M. & Rosas-Elguera, J., 2001. Ignimbrite flare-up and deformation in the southern Sierra Madre Occidental, western Mexico: implications for the late subduction history of the Farallon plate, *Tectonics,* **21,** doi:10.1029/2001TC001302.

Ferrari, L., Orozco-Esquivel, T., Manea, V. & Manea, M., 2012. The dynamic history of the Trans-Mexican Volcanic Belt and the Mexico subduction zone, *Tectonophysics,* **522–523,** 122–149.

Gao, W., Matzel, E. & Grand, S., 2006. Upper mantle seismic structure beneath eastern Mexico determined from P and S waveform inversion and its implications, *J. geophys. Res,* **111,** B08307, doi:10.1029/2006JB004304.

Gilbert, H.J., Sheehan, A.F., Dueker, K.G. & Molnar, P., 2003. Receiver functions in the western United States, with implications for upper mantle structure and dynamics, *J. geophys. Res.,* **108**(B5), doi:10.1029/2001JB001194.

Gómez-Tuena, A., LaGatta, A.B., Langmuir, C.H., Goldstein, S.L., Ortega-Gutiérrez, F. & Carrasco-Núñez, G., 2003. Temporal control of subduction magmatism in the eastern Trans-Mexican Volcanic Belt: mantle sources, slab contributions, and crustal contamination, *Geochem. Geophys. Geosyst.,* **4**(8), doi:10.1029/2003GC000524.

Gorbatov, A. & Fukao, Y., 2005. Tomographic search for missing link between the ancient Farallon subduction and the present Cocos subduction, *Geophys. J. Int.,* **160,** 849–854.

Gorbatov, A., Fukao, Y. & Widiyantoro, S., 2001. Application of a three-dimensional ray-tracing technique to global P, PP and Pdiff traveltime tomography, *Geophys. J. Int.,* **146,** 583–593.

Grand, S.P., van der Hilst, R.D. & Widiyantoro, S., 1997. Global seismic tomography: a snapshot of convection in the Earth, *GSA Today,* **7,** 1–7.

Gurrola, H. & Minster, J.B., 1998. Thickness estimates of the upper-mantle transition zone from bootstrapped velocity spectrum stacks of receiver functions, *Geophys. J. Int.,* **133,** 31–43.

Husebye, E.S., Chistoffersson, A. & Frasier, C.W., 1975. Orthogonal representations of array-recorded short period P-waves, in *NATO ASI Series, Series E: Applied Sciences, No. 11, Exploitation of Seismograph Networks,* pp. 297–309, ed. Beauchamp, K.G., Nordhoff.

Husker, A. & Davis, P.M., 2009. Tomography and thermal state of the Cocos plate subduction beneath Mexico City, *J. geophys. Res.,* **114,** B04306, doi:10.1029/2008JB006039.

Kanasewich, E.R., 1973. *Time Sequence Analysis in Geophysics,* The University of Alberta Press, 364 pp.

Kennett, B. & Engdahl, E.R., 1991. Travel times for global earthquake location and phase identification, *Geophys. J. Int.,* **105,** 429–465.

Kim, Y., Clayton, R.W. & Jackson, J.M., 2010. Geometry and seismic properties of the subducting Cocos plate in central Mexico, *J. geophys. Res.,* **115,** B06310, doi:10.1029/2009JB006942.

Li, X., Sobolev, S.V., Kind, R., Yuan, X. & Estabrook, Ch., 2000. A detailed receiver function image of the upper mantle discontinuities in the Japan subduction zone, *Earth planet. Sci. Lett.,* **183,** 527–541.

Li, C., van der Hilst, R.D., Engdahl, E.R. & Burdick, S., 2008. A new global model for P wave speed variations in Earth's mantle, *Geochem. Geophys. Geosyst.,* **9,** Q05018, doi:10.1029/2007GC001806.

Ligorría, J.P. & Ammon, C.J., 1999. Iterative deconvolution and receiver-function estimation, *Bul. seism. Soc. Am.,* **89,** 1395–1400.

Mammerickx, J. & Klitgord, K.D., 1982. Northern East Pacific rise: evolution from 25 m.y. B. P. to the present, *J. geophys. Res.,* **87,** 6751–6759.

MASE, 2007, Meso America subduction experiment. *Caltech. Dataset.* doi:10.7909/C3RN35SP.

Melgar, D. & Pérez-Campos, X., 2011. Imaging the Moho and subducted oceanic crust at the Isthmus of Tehuantepec, Mexico, from receiver functions, *Pure appl. Geophys.,* **168,** 1449–1460.

Morán-Zenteno, D.J., Cerca, M. & Keppie, J.D., 2007. The Cenozoic tectonic and magmatic evolution of southwestern Mexico: advances and problem of interpretation, *Geol. Soc. Am. Spec. Pap.,* **422,** 71–91.

Nieto-Samaniego, Á.F., Alaniz-Álvarez, A.S., Silva-Romo, G., Eguiza-Castro, M.H. & Mendoza-Rosales, C., 2006. Latest Cretaceous to Miocene deformation events in the eastern Sierra Madre del Sur, Mexico, inferred from the geometry and age of major structures, *Geol. Soc. Am. Bull.,* **118,** 238– 252.

Orozco-Esquivel, T., Petrone, C.M., Ferrari, L., Tagami, T. & Manetti, P., 2007. Geochemical and isotopic variability in lavas from the eastern Trans-Mexican Volcanic Belt: slab detachment in a subduction zone with varying dip, *Lithos,* **93,** 149–174.

Owens, T.J., Nyblade, A.A., Gurrola, H. & Langston, C.A., 2000. Mantle transition zone structure beneath Tanzania, East Africa, *Geophys. Res. Lett.,* **27,** 827–830.

Pardo, M. & Suárez, G., 1995. Shape of the subducted Rivera and Cocos plates in southern Mexico: seismic and tectonic implications, *J. geophys. Res.,* **100,** 12 357–12 373.

Pérez-Campos, X. & Clayton, R.W., 2013. Evidence of upper-mantle processes related to continental rifting versus oceanic crust in the Gulf of California, *Geophys. J. Int.*, **194,** doi:10.1093/gji/ggt133.

Pérez-Campos, X. *et al.*, 2008. Horizontal subduction and truncation of the Cocos Plate beneath central Mexico, *Geophys. Res. Lett.,* **35,** L18303, doi:10.1029/2008GL035127.

Rogers, R., Karason, H. & van der Hilst, R., 2002. Epeirogenic uplift above a detached slab in northern Central America, *Geology,* **30**(11), 1031–1034.

Schmandt, B., Dueker, K., Hansen, S., Jasbinsek, J. & Zhang, Z., 2011. A sporadic low-velocity layer atop the western U.S. mantle transition zone and short-wavelength variations in transition zone discontinuities, *Geochem. Geophys. Geosyst.,* **12,** 1–26.

Simmons, N.A. & Gurrola, H., 2000. Multiple seismic discontinuities near the base for the transition zone in the Earth's mantle, *Nature,* **405,** 559–562.

Song, T., Helmberger, D. & Grand, S., 2004. Low-velocity zone atop the 410-km seismic discontinuity in the northwestern United States, *Nature,* **427,** 530–533.

Tauzin, B., van der Hilst, R.D., Wittlinger, G. & Ricard, Y., 2013. Multiple transition zone seismic discontinuities and low velocity layers below western United States, *J. geophys. Res.,* **118,** 2307–2322.

van der Hilst, R.D., Widiyantoro, S. & Engdahl, E.R., 1997. Evidence for deep mantle circulation from global tomography, *Nature,* **386,** 578–584.

van der Lee, S. & Nolet, G., 1997. Seismic image of the subducted trailing fragments of the Farallon plate, *Nature,* **386,** 266–269.

VEOX, 2010. Veracruz-Oaxaca subduction experiment. *Caltech. Dataset.* doi:10.7909/C3MW2F2C.

Vinnik, L.P., 1977. Detection of waves converted from P to SV in the mantle, *Phys. Earth planet. Inter.,* **15,** 39–45.

Vinnik, L., Ren, Y., Stutzmann, E., Farra, V. & Kiselev, S., 2010. Observations of S410p and S350p phases at seismograph stations in California, *J. geophys. Res.,* **115,** 1–12.

Wessel, P. & Smith, W.H.F., 1991. Free software helps map and display data, *EOS, Trans. Am. geophys. Un.,* **72**(441), 445–446.

Yang, Y & Forsyth, D.W., 2006. Rayleigh wave phase velocities, small-scale convection, and azimuthal anisotropy beneath southern California, *J. geophys. Res.,* **111,** B07306, doi:10.1029/2005JB004180.

Yang, T., Grand, S.P., Wilson, D., Guzman-Speziale, M., Gomez-Gonzalez, J.M., Dominguez-Reyes, T. & Ni, J., 2009. Seismic structure beneath the Rivera subduction zone from finite-frequency seismic tomography, *J. geophys. Res.,* **114,** B01302, doi:10.1029/2008JB005830.

Zigone, D. *et al.*, 2012. Triggering of tremors and slow slip event in Guerrero, Mexico, by the 2010 Mw 8.8 Maule, Chile, earthquake, *J. geophys. Res.,* **117,** B09304, doi:10.1029/2012JB009160.

SUPPORTING INFORMATION

Additional Supporting Information may be found in the online version of this article:

Figure S1. a) Number of RFs per station. The various networks are distinguished (MASE, VEOX, MARS, GGAP, CONA, SSN). The number in parenthesis corresponds to the total RFs obtained for each network. The inset shows the distribution for each network of the semblance percentage between the estimated *Q* component (convolution of RF and observed *L* component) and the original *Q* component. The numbers in brown denote the percentiles 5, 25, 50, 75 and 95. This shows that more than 50 per cent of our RFs, when convolved with the *L* component reproduce at least 82 per cent of the observed *Q* component. b) Noise levels. Color shaded areas correspond to the 90 per cent of the median noise curves for each network. Black lines denote the new high-noise model (continuous) and new low-noise model (dashed) by Peterson (1993). The gray region represents the bandwidth we used for the RFs (0.025 – 0.3 Hz). c) Stacked RFs by ray parameter. Left: Unfiltered. Right: They have been filtered between 0.025 and 0.3 Hz. *P*410*s* (green arrows) and *P*660*s* (orange arrows) correspond to the theoretical arrival of the converted phase *P* to *S* at 410 km depth and at 660 km depth, respectively.

Figure S2. Azimuthal gap per node. It represents the largest azimuthal gap per node. In general, most events come from the SE, SW and NW, having the largest azimuthal gaps to the Northeast. The white line delimits the area within the nodes have an azimuthal gap less than 180°.

Figure S3. a) Position of profiles. b) Profiles along the direction of the slab subduction (1–16). Profiles 2, 4, 9, and 14 are shown in Fig. 3. Each RF shows the stack and its confidence interval. The brown areas correspond to the slab according to Yang *et al.* (2009) for profiles 1, 2, and 4, and to Husker & Davis (2009) for profile 9. Brown areas for profiles 5, 6, 7, 8, 10, and 11 denote our interpretation of the position of the slab, given similarities on the RFs with previous profiles. Brown areas in profiles 15 and 16 correspond to areas of cold material in tomography by Li *et al.*

(2008) that might correspond to a broken-off slab. Green areas denote regions of complex RFs. Black dashed lines denote our interpretation for the 410 and the 660. c) Profiles longitudinal to the slab (a-d). Brown area in profile d corresponds to cold material in tomography by Li *et al.* (2008) that might correspond to a broken-off slab. Green areas denote regions of complex RFs. Black dashed lines denote our interpretation for the 410 and the 660 (http://gji.oxfordjournals.org/lookup/suppl/doi:10.1093/gji/ggu087/-/DC1)

Please note: Oxford University Press is not responsible for the content or functionality of any supporting materials supplied by the authors. Any queries (other than missing material) should be directed to the corresponding author for the article.